Journal of The Electrochemical Society

The Electrochemical Society
Advancing solid state & electrochemical science & technology

OPEN ACCESS

# Morphology and Transport Characterization of Catalyst Layers for $CO_2$ Reduction

To cite this article: Francesca Lorenzutti and Sophia Haussener 2023 *J. Electrochem. Soc.* **170** 104507

View the article online for updates and enhancements.

You may also like

- Catalyst-Integrated Gas Diffusion Electrodes for Polymer Electrolyte Membrane Water Electrolysis: Porous Titanium Sheets with Nanostructured $TiO_2$ Surfaces Decorated with Ir Electrocatalysts
Masahiro Yasutake, Daiki Kawachino, Zhiyun Noda et al.
- Electrochemical Hydrogenation of CFC-12 at Metal-Phthalocyanine Supported Gas-Diffusion Electrodes
Noriyuki Sonoyama, Hideki Fujii and Tadayoshi Sakata
- Properties of Gas Diffusion Electrodes Containing Sulfonated Poly(ether ether ketone)
E. Bradley Easton, Toby D. Astill and Steven Holdcroft


This content was downloaded from IP address 128.179.253.183 on 14/12/2023 at 07:11

*Journal of The Electrochemical Society*, 2023 **170** 104507

# Morphology and Transport Characterization of Catalyst Layers for $CO_2$ Reduction

**Francesca Lorenzutti and Sophia Haussener**[z]

*Laboratory of Renewable Energy Science and Engineering, Institute of Mechanical Engineering, EPFL, 1015 Lausanne, Switzerland*

Gas diffusion electrodes (GDEs) help to reduce transport limitations in devices for electrochemical $CO_2$ reduction. Homogenized modeling of such devices requires input of morphological characteristics and effective transport properties of the porous structure, which can be obtained by pore-scale methods. Due to the small pore sizes and layer thicknesses, such characterization of the catalyst layer (CL) is difficult. In this work, CL structures digitalized by FIB-SEM nano-tomography were analyzed to obtain a set of morphological descriptors and were considered as geometrical domains in direct pore-scale simulations to calculate tensors of effective diffusion coefficient, permeability, tortuosity, and effective ionic and electronic conductivity. The CL properties vary significantly depending on the diffusion and flow direction, and samples of similar composition and synthesis technique exhibit different transport behaviors. The reported results provide a quantitative morphological analysis and a reliable set of effective properties to be used in homogenized device modeling, a net improvement over the most commonly used empirical or analytical formulations. The data set was obtained directly from the pore-scale structure of real CLs and contributes to making device-scale homogenized modeling of GDEs more accurate and reliable.

© 2023 The Author(s). Published on behalf of The Electrochemical Society by IOP Publishing Limited. This is an open access article distributed under the terms of the Creative Commons Attribution Non-Commercial No Derivatives 4.0 License (CC BY-NC-ND, http://creativecommons.org/licenses/by-nc-nd/4.0/), which permits non-commercial reuse, distribution, and reproduction in any medium, provided the original work is not changed in any way and is properly cited. For permission for commercial reuse, please email: permissions@ioppublishing.org. [DOI: 10.1149/1945-7111/acff1c]

Manuscript submitted June 23, 2023; revised manuscript received September 15, 2023. Published October 20, 2023.

The activity and selectivity of electrochemical devices depend on a series of chemical, transport and morphological factors:[1–3] for example, one principle dictates that higher specific surface area of the catalyst material leads to higher activity, therefore a common strategy in the design of electrocatalytic materials has been to increase the morphological complexity to obtain materials with a high specific surface.[4] Increasing the concentration of the reactant at the interface also leads to higher activity, therefore another guiding principle aims at overcoming transport limitations by reducing the diffusion path length of reactants. Gas Diffusion Electrodes (GDEs) have been developed for this purpose and are particularly relevant to help reduce transport limitations in devices for $CO_2$ reduction reaction ($CO_2$RR), given the low solubility of $CO_2$ in aqueous electrolytes. In GDE based devices, gaseous $CO_2$ is transported in the vicinity of the porous Catalyst Layer (CL) through a Gas Diffusion Layer (GDL), which is usually composed of carbon fibres and characterized by a stochastic, complex morphology. The combination of CL and GDL constitutes the GDE. GDEs used to perform $CO_2$RR have emerged as prime candidate for electrochemical $CO_2$RR devices with industrially relevant current densities.[5,6] As highlighted by Ref. 7, homogenized modeling of $CO_2$RR devices incorporating porous electrodes such as GDEs is an important approach allowing to account for all the relevant physical processes taking place in electrochemical devices. It allows to reasonably reproduce (or predict) the behavior of complex devices with low computational effort,[8,9] to systematically test different operating conditions[10] and geometrical configurations in order to develop physics-based design guidelines, avoiding the numerical complexity of pore-scale modeling.[11] These homogenized models rely on effective transport properties—such as tortuosity, effective diffusion coefficient or permeability—typically obtained from approximate analytical formulations. Such formulations have the advantage of being extremely straightforward to derive, as they depend only on few simple descriptors like porosity, but they fail to take into account the influence of local morphological characteristics of the pore-scale structure on the transport properties.[12] Furthermore, the anisotropic characteristics of the GDEs pore-scale structure in devices for $CO_2$RR are not considered.

Tomography-based techniques provide precise information on the pore-scale structure of materials. In particular, focused ion beam-scanning electron microscopy (FIB-SEM) tomography can resolve materials at the mesoscale down to 4 nm, the lengthscale of interest for materials of (photo)electrochemical applications.[13,14] Digitalized representations of the materials were obtained from such characterization, and this geometrical domains were then used to carry in-depth morphological characterization in order to extract relevant, representative and quantitative morphological descriptors. The obtained information was used to estimate transport parameters through analytical relations. Furthermore, pore-scale transport simulations were directly carried out on the relevant domains in order to obtain effective transport properties calculated by explicitly taking into account the exact pore-scale structures, including their anisotropic characteristics. We applied this methodology for in-depth morphological characterization of CL for $CO_2$RR and for the direct pore-scale extraction of quantitative morphological characteristics and effective transport properties. A set of morphological properties and tensors of effective transport properties obtained by direct pore-scale simulations are reported. They constitute a reliable dataset for device-scale simulations.

## Methods

***Digitalization of catalyst layers.***—Three metallic CLs for $CO_2$RR deposited on GDLs were considered. Two sputtered Cu based CL were selected in consideration of their similar composition and standard synthesis technique: the first sample (DTU-Cu) was produced at the Technical University of Denmark (DTU) and consists of 150 nm of Cu sputtered on DeNora DN908 GDL;[15,16] the second (TUDelft-Cu) was produced at Delft University of Technology and consists of 100 nm of Cu sputtered on a Sigracet 38BC GDL.[17] A third CL, obtained via a particle deposition technique, was included: UBern-Ag was produced at the University of Bern and consists of 40 $\mu g/cm^2$ of airbrushed Ag nanowires on a Sigracet 39BC GDL.[18] Detailed synthesis procedures are reported in the corresponding papers. We expect different physical properties to arise from the different composition, load, synthesis technique and support. The reference frame for the three CLs is fixed such that the $x$ and $z$ axis are parallel to the GDL support, while the $y$ axis is perpendicular to the GDL deposition plane and correspond to the direction of the $CO_2$ flow in the GDE.

[z]E-mail: sophia.haussener@epfl.ch

The catalyst layers were characterized via FIB-SEM nano-tomography. The materials are progressively FIB-milled along the $z$ direction, and the $xy$ planes are imaged via a SEM column, allowing to reconstruct a 3D volume.[19] Characterizing C-based materials (such as the mesoporous layer or ionomers that might be present in the CL) is challenging because the samples are embedded in epoxy, which is itself C-based. To characterize in a satisfactory way both the characteristic features of the electrodes and a sufficiently large volume, DTU-Cu and TUDelft-Cu were recorded with a voxel size of 4 nm, while UBern-Ag was recorded with a voxel size of 8 nm. Sample preparation and image acquisition followed the methodology detailed in Ref. 13. Nano-tomography experiments were carried out on a Zeiss NVision 40 CrossBeam (electron-beam: ZEISS Gemini, 1-30 kV, 1 nm@30 kV, 2.5 nm@1 kV; ion-beam: 1-30 kV Ga liquid metal ion source, 4 nm@30 kV). The stacks of greyscale images (specifically, backscattered electrons images) resulting from the tomography experiments were converted into digitalized materials through a segmentation process consisting in 1) image alignment and contrast balancing, 2) selection of an ideal threshold based on visual assessment of accuracy, as well as a conservative and an aggressive thresholds to fix a confidence interval, and 3) 3D morphological opening operation (structuring element $d = 3$ voxels) to smooth the surface of the materials.[20] All the segmentation and morphological characterization procedures are performed with Matlab2017b. The digitalized structures are obtained in the form of a binary 3D tensor.

***Morphological characterization.—***A series of quantitative and representative morphological information can be retrieved from the digitalized CLs, namely, the solid volume fraction, $\phi$, and the porosity, $\varepsilon$. Additionally, locally resolved information such as the volume fraction profile $\phi(y)$, describing how (in)homogeneously the catalyst material is distributed in space, can be obtained by calculating the volume fraction moving along through plane direction (corresponding to the $y$-axis in our reference frame). The GDE support on which the CLs are deposited is not perfectly flat, therefore it was difficult to quantify their thickness: the boundaries of the CLs were taken to be the $y$-values for which the volume fraction goes to zero at the two extremes of the volume fraction profile curve. The percentage of connected volume is calculated considering 16-connectivity via a watershed algorithm (Matlab function "bwconncomp"). The total surface area was obtained by triangulating the CLs interface through the Matlab function "isosurface", as well as the surface meshes necessary to start the volume mesh procedure. The roughness factor was obtained by normalizing this result with respect to the equivalent geometric area of the CLs. The chord length distribution was obtained by measuring the length of the chords of the CLs, going from one void-solid interface to the next solid-void interface. The operation was repeated along the three Cartesian directions in order to quantify the anisotropy of the samples. The size distribution of the CLs were calculated based on a series of morphological opening operations with spherical structuring elements (SEs).[13] The morphological characterization procedure was also performed on the digitalized CLs obtained with conservative and aggressive segmentation to quantify the influence of the selected threshold values on the results and to obtain confidence intervals. The smaller SE has a diameter of 3 voxels, therefore the minimum quantifiable particle size is limited by the tomography resolution: 12 nm for DTU-Cu and TUDelft-Cu and 24 nm for UBern-Ag.

***Two-point correlation and representative volume element.—***The resolution in a FIB-SEM tomography experiment allows to acquire volumes from about 65 $\mu m^3$ to 125 $\cdot 10^6$ $\mu m^3$.[19] Conducting computations investigating transport at the mesoscale on such large domains would be an unnecessary computational effort, as the extracted pore-scale information would be redundant. Developing and applying a rigorous technique to select a suitable representative volume element (RVE), defined as a subsection of a material that retains all its relevant transport and morphological properties, is imperative. The methodology we adopted was based on Refs. 21, 22 and used the two-point solid-solid correlation function to select a RVE among a set of subvolumes of a given dimension. The RVE was selected among a set of subvolumes as the subvolume with two-point correlation closest to the average of the sample. The two-point solid-solid correlation is defined as the combined average probability of randomly choosing two points in a sample and finding them both in the solid phase.[23]

The minimum possible size of the RVE depends on the specific sample and on the property under investigation. Here, the size of the subvolumes in the set must be large enough to include all the characteristic features of the CLs. This was ensured by verifying the morphological properties converge to their values of the full sample: each subvolume undergo morphological characterization—$\varepsilon$, $\phi$, $\phi(y)$ and average particle diameter distributions were obtained. The number of subvolumes was chosen to be sufficiently large to sample the full volume at least three times.

***Review of analytical correlations of morphological and transport properties.—***A number of analytical formulations to estimate morphological characteristics and effective transport properties based on simple descriptors of the material's morphology (such as porosity) exist. Such models often rely on assumptions on the geometry of the material of interest: the radius of the particles composing the CL and the porosity are often chosen a priori; furthermore, isotropy is assumed.

The interface area per unit volume is estimated starting from $\varepsilon$ and the radius $r$ of the particles and assuming a CL composed by spherical particles loosely packed in a simple cubic structure.[8]

$$a_v = \frac{3(1-\varepsilon)}{r}. \quad [1]$$

The roughness factor can be estimated as $a_v \cdot h$, where $h$ is the thickness of the catalyst layer. The catalyst volume per unit geometric area can also be deduced:

$$V_a = \frac{h(1-\varepsilon)}{3} \cdot \sqrt[3]{\frac{(1-\varepsilon)}{4\pi/3}}. \quad [2]$$

Tortuosity $\tau$ is often related to the porosity of the medium, for example by the Maxwell formulation[24] ($\tau_M^2 = 0.5(3-\varepsilon)$) and the Bruggeman formulation[25,26] ($\tau_B^2 = \gamma\varepsilon^{1-\alpha}$). $\gamma$ and $\alpha$ can be fitted to specific experimental data points, but are usually taken as $\gamma = 1$ and $\alpha = 1.5$.[24]

Permeability $K$ is often given as function of $\varepsilon$ and specific surface area, with geometry-dependent constants. According to Carman-Kozeny theory, permeability can be formulated as in Eq. 3a, with $d$ the average particles diameter.[27] $k_K = k_0\tau^2$ is the Kozeny constant, usually taken to be 5 (assuming $\tau = \sqrt{2}$ and $k_0 = 2.5$ specifically). Rumpf and Gupte[28] derived a different formulation (Eq. 3b) for packed beds of monodispersed spheres. In the case of fibrous beds,[29] often characterized by high porosity, Davies suggested the formulation in Eq. 3c, with $a = 64$, $b = 56$ for $\varepsilon < 0.98$, and $a = 70$, $b = 52$ otherwise. Another formulation for fibrous beds by Chen[30] isgiven in Eq. 3d.

$$K_{CK} = \frac{\varepsilon^3 d^2}{36 k_K \phi^2}. \quad [3a]$$

$$K_{RG} = \frac{\varepsilon^{5.5} d^2}{5.6}. \quad [3b]$$

$$K_{Davies} = \frac{d^2}{a\phi^{3/2}\cdot(1 + b\phi^{3/2})}. \quad [3c]$$

$$K_{\text{Chen}} = \frac{\pi e d^2 \ln(0.64/\phi^2)}{24.4 \cdot \phi}. \quad [3d]$$

The normalized effective diffusion coefficient $D_{\text{eff}}/D$ is often calculated as in Eq. 4, although Epstein Ref. 31 pointed out that this formulation was originally derived for a bundle of sinuous capillaries and it is therefore not suitable to estimate values for other geometries, such as randomly packed spheres.

$$\frac{D_{\text{eff}}}{D} = \frac{\varepsilon}{\tau^2}. \quad [4]$$

The effective conductivity of a porous material saturated with an electrolyte can be described by the Macmullin number $N_M$.[32,33] A common formulation,[24] equivalent to the reciprocal of Eq. 4, is given in Eq. 5a. For random arrangements of monodispersed spheres, Meredith and Tobias derived Eq. 5b,[32] and for a random arrangement of fibers, Tomadakis and Sotirchos[34] proposed Eq. 5c.

$$N_M = \frac{\tau^2}{\varepsilon}. \quad [5a]$$

$$N_{M\,\text{spheres}} = \frac{(5-\varepsilon)(3+\varepsilon)}{8(1+\varepsilon)\varepsilon}. \quad [5b]$$

$$N_{M,\text{fibers}} = \frac{0.9126}{\varepsilon(\varepsilon - 0.11)^{0.785}}. \quad [5c]$$

To estimate the normalized effective electronic conductivity of a porous solid domain $\sigma^e_{\text{eff}}$, $\varepsilon$ was substituted with $\phi$ in Eq. 4.[35] The solid phase tortuosity $\tau_s$ was estimated considering both Maxwell and Bruggeman formulations. Considering that the effective electronic conductivity in the solid phase is equivalent to the effective diffusion coefficient in the fluid phase, $\sigma^e_{\text{eff}}/\sigma^e$ was estimated as:

$$\frac{\sigma^e_{\text{eff}}}{\sigma^e} = \frac{\phi}{\tau_s^2} \quad [6]$$

Morphological information obtained from the subvolumes sets sampled for the RVE selection were used to estimate effective transport properties for all the CLs. The results of both morphological characterization and effective property estimation for the three sets were fitted on Gaussian distributions, a Kolmogorov-Smirnov (KS) goodness of fit test with decision level 5% was performed to verify the normal hypothesis on each set of results. The mean and the standard deviation are given for each calculated quantity.

***Transport simulations.***—Tensors of transport properties are symmetric and diagonal when considering the principal axis of orthotropic media.[27] For the considered materials, we assume that the principal axes are two orthogonal axes ($x$ and $z$) parallel to the CL and one (the $y$ axis) perpendicular to it and parallel to the hypothetical $CO_2$ inlet flow. We expect anisotropy along the $y$ direction: UBern-Ag is composed by rods, and it is natural to expect that they will lie horizontally once deposited, leading to anisotropy along the $y$ axis. TUDelft-Cu and DTU-Cu are sputtered on a porous support, therefore we expect the results of deposition to be different along the $y$ axis than on the $xz$ plane. To investigate the anisotropy in transport, each RVE was meshed three times, resulting in three geometrical domains with inlet and outlet with length about three times the RVE thickness - 6 $\mu$m length for DTU-Cu and TUDelft-Cu and 12 $\mu$m length for UBern-Ag - aligned along the three Cartesian directions. The tensors $\mathbf{K}$, $\boldsymbol{\tau}$, $\mathbf{D}_{\text{eff}}/D$ and $\boldsymbol{\sigma}^e_{\text{eff}}/\sigma^e$ for the three CLs were extracted with this approach, allowing to quantify anisotropy. The RVEs in the form of a surface mesh served as input for the blockMesh and snappyHexMesh tools in the openFOAM open-source software package,[36] which was used to generate unstructured meshes consisting of hexahedral cell elements. These channels were also used to calculate fluxes in the diffusivity and conductivity simulations and to allow for the flow to stabilize in laminar flow simulations. For each sample, a mesh study was carried out to ensure the independence of the simulation results on mesh elements density. The three final RVE meshes (inlet along $x$, $y$ and $z$, respectively) were in the order of 50 million hexahedral mesh elements for UBern-Ag, with the biggest mesh element measuring $2.9 \cdot 10^5$ nm$^3$ and the smallest 0.48 nm$^3$; and 80 million elements for TUDelft-Cu, the biggest element being $3.1 \cdot 10^5$ nm$^3$ and the smallest 0.40 nm$^3$. Concerning DTU-Cu, its complex morphology, characterized by higher roughness, wider particle size distribution and higher thickness with respect to the other samples, required a higher number of mesh elements in order to obtain results independent on the mesh density. Due to memory limitations, the RVE was split in two and two meshes with number of elements in the order of 75 million were produced for each Cartesian direction. The biggest mesh element was $3.0 \cdot 10^5$ nm$^3$ and the smallest one 0.18 nm$^3$. The simulation results for DTU-Cu are reported as average of two simulations with a standard deviation.

The relevant governing pore-scale conservation and transport Eqs. were solved in these domains with results relative to the considered transport direction. All the simulations were carried out assuming a continuum fluid; in particular, small Knudsen numbers and incompressible fluids were assumed.

First, the pore-resolved pressure and velocity vector fields were used to calculate via Darcy's law the effective permeability tensor $\mathbf{K}_{\text{eff}}$ and the tortuosity tensor $\boldsymbol{\tau}$. 225 streamlines per $\mu$m$^2$ were calculated for each sample and direction starting from the inlet plane and their length distributions was recorded to extract the correspondent tortuosity tensor component ($\tau = \frac{L_{path}}{L_p}$). Finally, the tortuosity relative to the considered flow direction ($\tau_x$, $\tau_y$ and $\tau_z$) was taken as the average of the distribution.

Subsequently, the superficial velocity was set to zero and the pore-resolved concentration fields, obtained by setting appropriate boundary conditions at the inlet and outlet, were used to calculate via Fick's law the normalized effective diffusion coefficient tensor $\mathbf{D}_{\text{eff}}/D$. A migration term must be included to describe the ionic transport phenomena in stagnant fluids. Ionic conductivity due to diffusion $\boldsymbol{\sigma}^D$ and migration $\boldsymbol{\sigma}^m$ across a porous media only depend on the diffusion coefficient of the species $i$, $\mathbf{D}_i$, and on some constants. Therefore, the normalized effective ionic conductivity can be deduced:

$$\frac{\boldsymbol{\sigma}^D_{\text{eff}}}{\sigma^D} = \frac{\boldsymbol{\sigma}^m_{\text{eff}}}{\sigma^m} = \frac{\boldsymbol{\sigma}_{\text{eff}}}{\sigma} = \frac{\mathbf{D}_{\text{eff}}}{D}. \quad [7]$$

The Macmullin number introduced in the previous section (Eq. 5) corresponds to the reciprocal of the normalized effective ionic conductivity in Eq. 7.

Finally, the solid domain was considered (the inlet and outlet regions of all the geometrical domains were considered as part of the solid domain) and the pore-scale resolved potential field, obtained by setting appropriate boundary conditions at the inlet and outlet, was used to derive the solid effective electrical conductivity tensor $\boldsymbol{\sigma}^e_{\text{eff}}$ via Ohm's law.

Simulations are set up on Ansys Fluent 2021 R1 and are run on a 210-AKWU PowerEdge R640 Server mounting two Intel Xeon Gold 6248R processors (3 GHz, 24C/48T, 10.4 GT/s, 205 W), and 376 GB DDR4 RAM (2933 MHz). Typical calculation times are about 6 h for each simulation and each geometrical domain.

## Results and Discussion

***Morphological characterization.***—Information on the resolution and the corresponding dimensions in $\mu$m of the digitalized CL are summarized in Table I. The 3D rendering of the structures in Fig. 1,

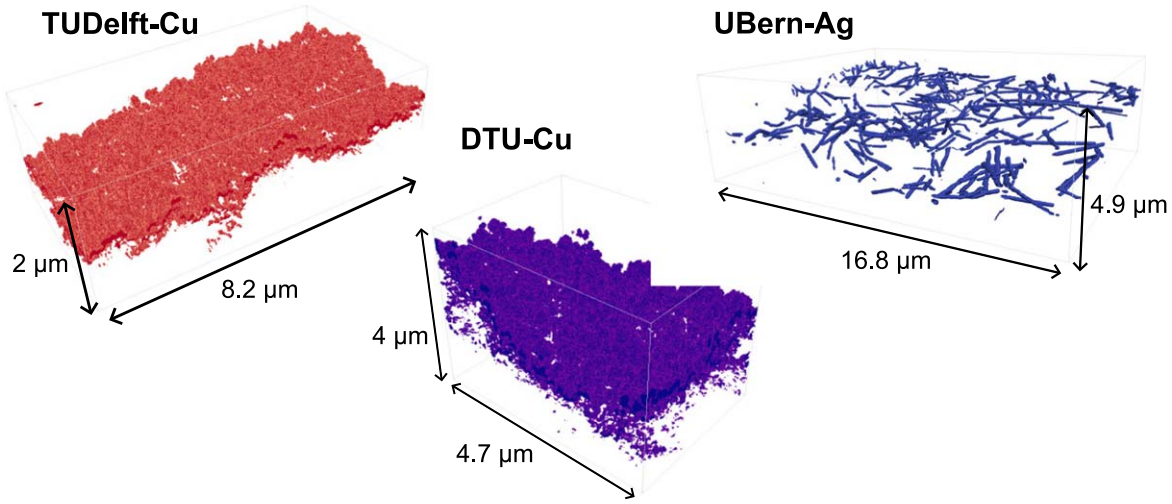


**Figure 1.** 3D visualization of the segmented stacks, from left to right: TUDelft-Cu, DTU-Cu and UBern-Ag. For TUDelft-Cu and UBern-Ag the whole CL stack is shown, in the case of DTU-Cu a reduced volume is rendered for better visualization. The thickness bar refers to the represented image stack thickness and not to the thickness of the CLs, and is added for ease of visualization.

**Table I. Dimension of the 3D binary tensors containing the structural information relative to the three CLs in volxels, and the corresponding dimensions in $\mu$m based on the FIB-SEM resolution.**

| | $x$ (voxels) | $y$ (voxels) | $z$ (voxels) | Resolution | $x$ ($\mu$m) | $y$ ($\mu$m) | $z$ ($\mu$m) |
|---|---|---|---|---|---|---|---|
| UBern-Ag | 1622 | 620 | 2102 | 8 nm | 13.0 | 4.9 | 16.8 |
| TUDelft-Cu | 2059 | 1121 | 1143 | 4 nm | 8.2 | 4.5 | 4.6 |
| DTU-Cu | 2485 | 1763 | 1899 | 4 nm | 9.9 | 7.1 | 7.6 |

**Table II. Collection of morphological information from the characterization of the segmented materials. The confidence intervals are derived from morphological characterization of the structures obtained through the conservative and aggressive segmentation procedures.**

| | UBern-Ag | TUDelft-Cu | DTU-Cu |
|---|---|---|---|
| Solid volume per geometric area ($\mu$m) | 0.029 ± 0.002 | 0.16 ± 0.02 | 0.30 ± 0.02 |
| Volume fraction $\phi$ | 0.0069 ± 0.0004 | 0.059 ± 0.006 | 0.046 ± 0.004 |
| Porosity $\varepsilon$ | 0.9931 ± 0.0004 | 0.941 ± 0.006 | 0.954 ± 0.004 |
| Roughness factor | 1.00 ± 0.03 | 7.9 ± 0.5 | 15.0 ± 0.8 |
| Average particle diameter (nm) | 126 ± 3 | 85 ± 3 | 92 ± 2 |
| Connected solid volume % | 24.29 ± 0.01 | 97.31 ± 0.05 | 92 ± 1 |

obtained with the open-source program Tomviz,[37] allow for a visual comparison between the CLs: the rendering of TUDelft-Cu CL shows an overall flat layer of material with some voids on the deposition plane, while the DTU-Cu CL appears to be more morphologically complex, 3-dimensional, and to contain overall more solid material. A comparison between the solid volume per geometric area for the two samples in Table II shows that the volume of Cu deposited per unit area for the DTU-Cu sample is almost double compared to the TUDelft-Cu (0.30 $\mu$m vs 0.16 $\mu$m). The same is observed for the roughness factor (7.9 vs 15.0). Cu is distributed differently in the two samples, as can be seen in Fig. 2a: TUDelft-Cu reaches a peak of volume fraction of 0.2 in a narrow depth interval of 2 $\mu$m; while DTU-Cu never goes over a volume fraction of about 0.15 but the CL reaches a thickness of about 5.5 $\mu$m. Therefore, $\phi$ in the CLs is 22% lower for DTU-Cu ($\phi = 0.046$) compared to TUDelft-Cu ($\phi = 0.059$). Consequently, TUDelft-Cu has a lower $\varepsilon$ compared to DTU-Cu ($\varepsilon = 0.941$ vs 0.954). Concerning the average particle diameter, calculated from the data in Figs. 2c and 2d, TUDelft-Cu exhibits $d = 85$ nm, 8% (7 nm) smaller than DTU-Cu, which presents an average particle diameter of 92 nm. UBern-Ag CL 3D rendering in Fig. 1 shows a highly porous material and a low surface coverage. Indeed, the total volume per geometric area (0.029 $\mu$m) is one order of magnitude lower than for DTU-Cu and TUDelft-Cu, and the roughness factor, equal to 1, is also the lowest in the set, equivalent to only 7% of the DTU-Cu value. Nevertheless, the average particle diameter of 125.5 nm is the biggest in the set, and the volume fraction profile in Fig. 2b shows that the material is quite thick (about 4 $\mu$m), indicating a somewhat complex morphology despite the very low quantity of deposited Ag and the peak volume fraction being about 0.02. $\phi$ for this CL is extremely low, only 0.0069, and $\varepsilon$ is the highest in the set, 0.9931. Furthermore, the biggest connected subsection of the CL only includes 24.29% of the solid volume, as compared to DTU-Cu, where the biggest connected volume is 92% of the total Cu volume, and TUDelft-Cu, where 97.31% of the total volume is connected.

It is possible to estimate the roughness factor and the volume per geometric area from Eqs. 1 and 2 and considering the CLs thicknesses, $\varepsilon$ and the particle diameters. The estimated roughness factors are 8.3 for TUDelft-Cu, 15 for DTU-Cu and 1.3 for UBern-Ag. The roughness for TUDelft-Cu and UBern-Ag are slightly higher compared to the direct pore-scale results, while the estimation

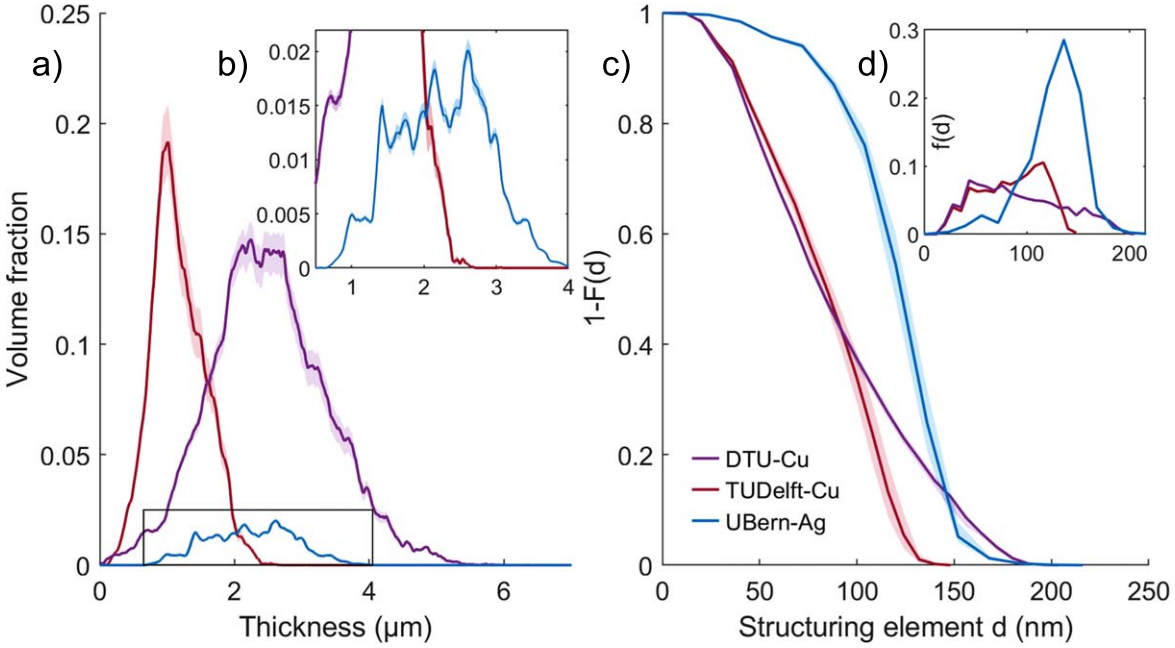


**Figure 2.** (a) Volume fraction profiles of UBern-Ag, TUDelft-Cu and DTU-Cu samples. The shaded areas represent the confidence interval given by the analysis of the structures resulting from the aggressive and conservative segmentations. (b) Highlight of the volume fraction profile of UBern-Ag and its confidence interval. (c) $1 - F(d) = \phi(d)/\phi_0$, with $F(d)$ the cumulative size distribution, $\phi(d)$ the volume fraction after opening with structuring element of diameter $d$ and $\phi_0$ the CL volume fraction. (d) Particle size distribution $f(d) = F'(d)$.

for DTU-Cu in in perfect agreement with the pore-level calculation based results, even though the assumptions on the geometry (simple packing of spherical catalyst particles) are not a good approximation of the actual morphology of the CLs. Concerning the total volume per geometric area, the estimation gives 0.0098 $\mu$m for for TUDelft-Cu, 0.018 $\mu$m for DTU-Cu and 0.0011 $\mu$m for UBern-Ag. All values are lower compared to the pore-level simulation based results: the local porosity and thickness of the CLs are both lower than the global ones considered in the estimates.

The maximum length of chords in the CLs is around 1.5 $\mu$m for UBern-Ag and 1 $\mu$m for both TUDelft-Cu and DTU-Cu (see Fig. 3). All the samples exhibit anisotropy: the behavior along the $x$ and $z$ direction (parallel to the GDL support) is equivalent while the chords in the $y$ direction are shorter. The longest chords along the $y$ direction are about 0.6 $\mu$m for UBern-Ag, and 0.5 $\mu$m for TUDelft-Cu, denoting respectively a decrease of 40% and 50% with respect to $x$ and $z$ directions in the two samples. DTU-Cu exhibits a less pronounced anisotropic behavior, with the longest chords along the $y$ direction showing some components reaching 0.85 $\mu$m, denoting a 8.5% difference with respect to the $x$ and $z$ directions. Overall, the chord length distribution supports the orthotropic assumptions adopted in the transport simulations. We expect differences in the transport properties of the CLs depending on the considered main axis, consistently with the anisotropy predictions here.

***Two-point correlation and representative volume element.—*** The subvolumes chosen for the RVE determination were sampled considering the average particles diameter and maximum chord length ($x$ and $z$ directions). The full thickness of the CLs ($y$ direction) was always included. In the case of TUDelft-Cu and DTU-Cu samples, a size of 2 $\mu$m (i.e. 500 voxels) in the $x$ and $z$ directions—corresponding to twice the length of the longest chords and more than 20x the average particle diameter—was considered. Concerning the UBern-Ag sample, a size of 4 $\mu$m (i.e. 500 voxels) in the $x$ and $z$ directions was selected. This is more than twice the longest chords and more than 30x the particle diameter, allowing to account for the higher porosity of the UBern-Ag sample. We chose 60 subvolumes, ensuring a sampled geometric area in the $xz$ plane of 3x the equivalent geometric area of DTU-Cu, which is the largest binary 3D tensor (see Table I), allowing to appropriately sample all the morphology with a random choice of the subvolumes in the $xz$ plane.

Morphological characterization is carried on the three sets of subvolumes. Results of morphological characterization, including $\varepsilon$, $\phi$ and average particles diameter in the three CLs, are gathered in Table III. The confidence intervals of morphological descriptors, obtained by fitting over the subvolumes sets, are larger than the ones computed considering the aggressive and conservative thresholds in Table II, highlighting that there are local variations in morphological properties with respect to the average that are more relevant than variations due to the segmentation threshold (see Fig. 4). The average values for $\phi$ and $\varepsilon$ are, respectively, higher and lower than the ones calculated on the full sample: the set average $\varepsilon$ is 1% lower than total for UBern-Ag and 4% lower than total for TUDelft-Cu and DTU-Cu. Owing to its low values, $\phi$ percentage variation is more accentuated: $\phi$ set average is 58% higher than the total sample $\phi$ for TUDelft-Cu, 74% higher for DTU-Cu and 175% higher in UBern-Ag. This can be explained by the fact that $\phi$ was calculated for each subvolume by averaging over the volume fraction profile, meaning that the local thickness of the material was taken into consideration, rather than the global one. Since the GDL support is not perfectly flat, when calculating $\phi$ and $\varepsilon = 1 - \phi$ for the total sample some extra void phase was considered. Concerning the average particle diameter, there is a very good agreement with the values and confidence intervals in Table II and in Table III: all the three sets average fall within the confidence interval of the sample average, with the biggest difference being of only 0.5 nm in UBern-Ag. This confirms that the selected subvolumes dimension is appropriate to represent the morphological features of all the CLs.

The morphological property variations of the selected RVEs with respect to the set average is minimal for all the three CLs. The difference in the average diameter of the RVE with respect to the average is below 2% for the three samples. The difference in $\phi$ with respect to the average is 3% for UBern-Ag and 7% for TUDelft-Cu. $\phi$ in DTU-Cu RVE is 21% higher than the sample average. The RVE is selected to maintain methodological uniformity and in consideration of the fact that the RVE choice through the two-point correlation should account for more complex morphological descriptors than the simple volume fraction.

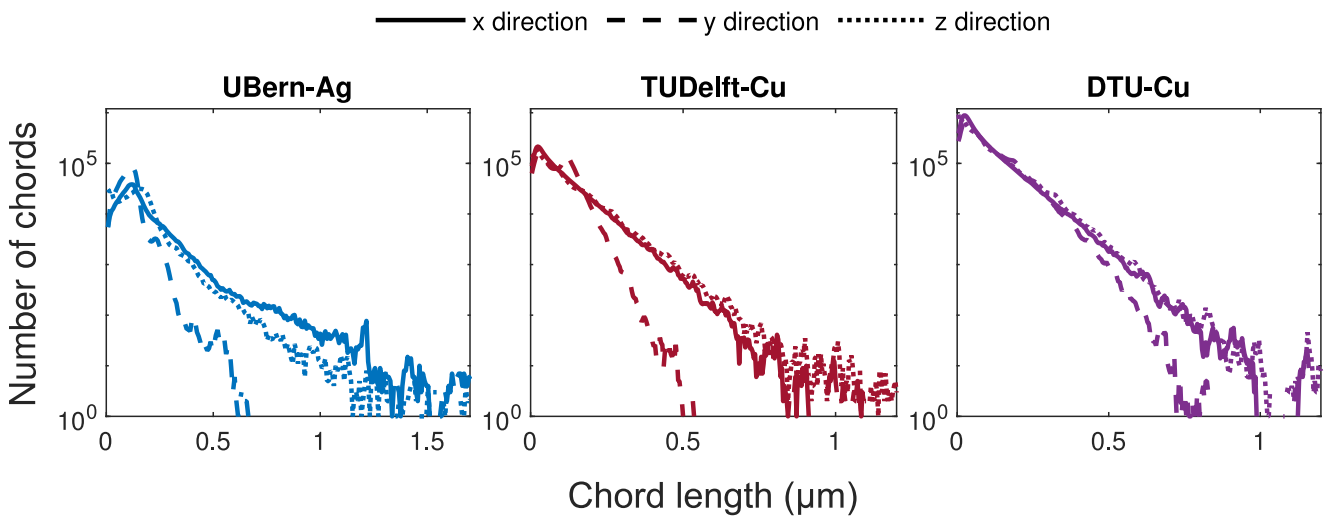


**Figure 3.** Chord length distributions in the *x*, *y* and *z* direction for UBern-Ag, TUDelft-Cu and DTU-Cu samples. Anisotropy can be observed for the chord length distributions along the *y* direction.

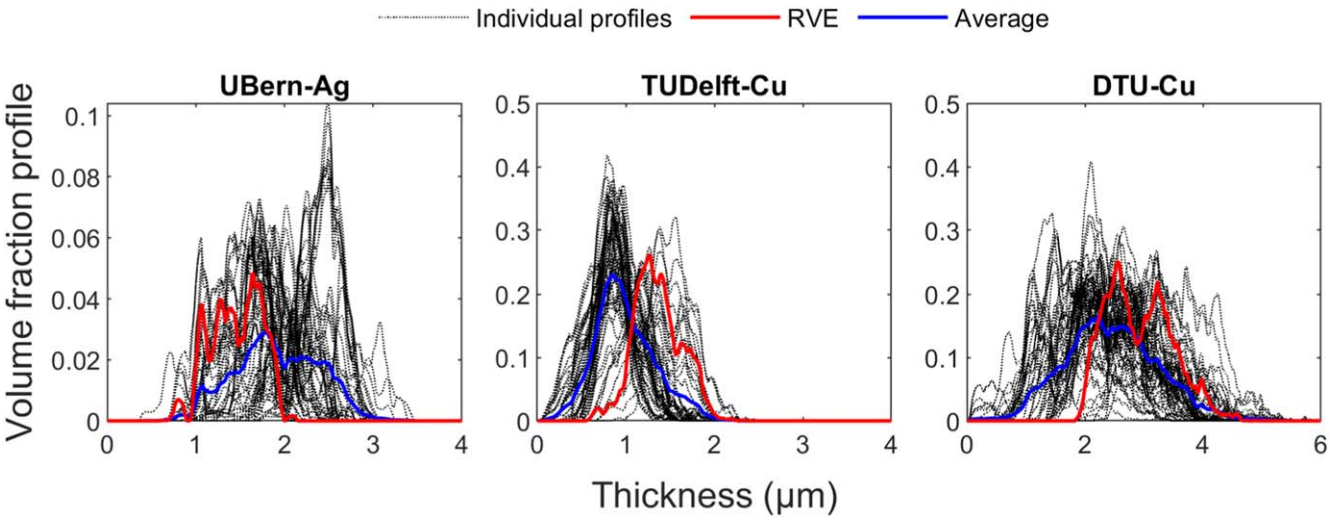


**Figure 4.** Collection of the volume fraction profiles for the subvolumes sets of UBern-Ag, TUDelft-Cu and DTU-Cu samples. The bold, blue lines are the volume fraction average of the corresponding sample, the bold, red lines are the volume fraction of the selected RVEs.

**Table III. Results of the morphological characterization conducted on the set of subvolumes for each CL. The average and standard deviation for each properties is reported, together with the corresponding value for the selected RVE.**

| | UBern-Ag | | TUDelft-Cu | | DTU-Cu | |
|---|---|---|---|---|---|---|
| | Ensemble | RVE | Ensemble | RVE | Ensemble | RVE |
| Volume fraction $\phi$ | 0.019 ± 0.007 | 0.0185 | 0.093 ± 0.008 | 0.0864 | 0.08 ± 0.01 | 0.0946 |
| Porosity $\varepsilon$ | 0.981 ± 0.007 | 0.9815 | 0.907 ± 0.008 | 0.9136 | 0.92 ± 0.01 | 0.9054 |
| Avg. diameter (nm) | 126 ± 4 | 123.4 | 85 ± 2 | 84.49 | 92 ± 3 | 92.28 |

***Effective transport properties.—***$\tau$ calculated considering the subvolumes sets and the RVEs with the Maxwell and the Bruggeman formulations are reported in Table IV. The $\tau$ values calculated according to the two analytical expressions vary significantly, while variations among the samples are smaller. The largest $\tau_B = 1.025 \pm 0.002$ is the one of TUDelft-Cu, given that it is the sample exhibiting lower $\varepsilon$. When considering the RVEs, the largest $\tau_B = 1.025$ is from DTU-Cu, 0.4% more than the mean of $1.021 \pm 0.003$, while for TUDelft-Cu $\tau_B = 1.023$ for the RVE. As expected by its high $\varepsilon$ value, the sample with lowest $\tau_B = 1.005 \pm 0.002$ is UBern-Ag, only about 2% lower than TUDelft-Cu; its $\tau_B = 1.005$ for the RVE. In turn, when considering the Maxwell formulation, UBern-Ag exhibits a mean $\tau_M = 1.584 \pm 0.001$, which is 58% higher than $\tau_B$. The largest mean $\tau_M = 1.596 \pm 0.001$ is again calculated for TUDelft-Cu, and it is only 0.8% larger than UBern-Ag. When considering the RVEs, the largest $\tau_M = 1.596$ is from DTU-Cu, which is 0.2% larger than the corresponding mean of $\tau_M = 1.593 \pm 0.002$. The Maxwell formulation predicts $\tau_M$ of almost 1.6 for all the CLs. This indicates an overestimation, especially in the case of the high-porosity UBern-Ag

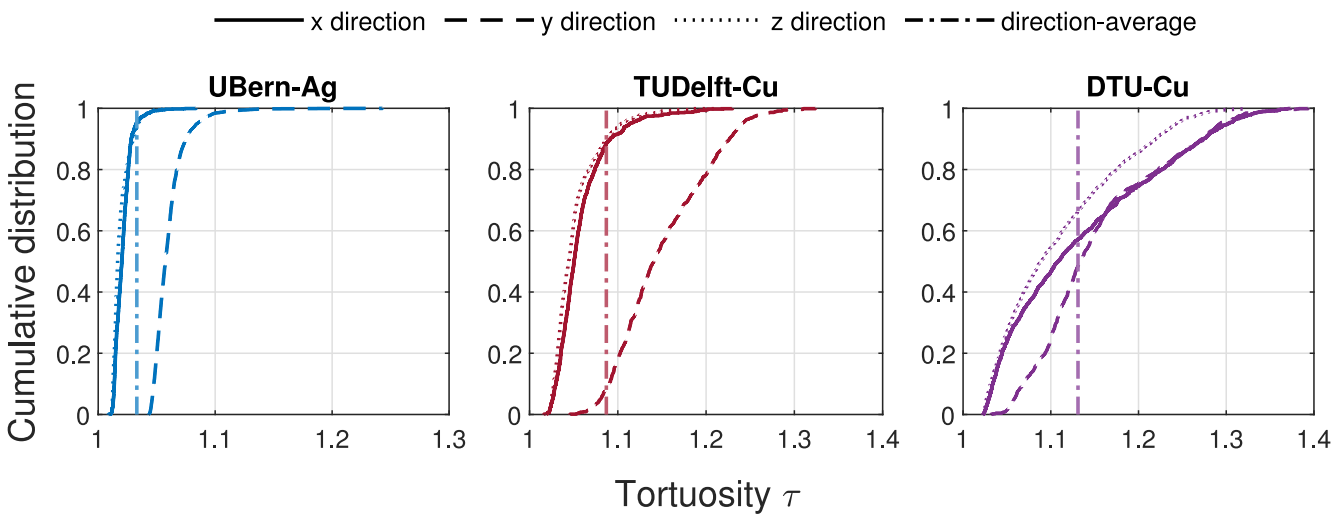


**Figure 5.** UBern-Ag, TUDelft-Cu and DTU-Cu samples' tortuosity cumulative distribution along $x$, $y$ and $z$ directions directly calculated from fluid flow simulations. The vertical lines represents the direction-averaged $\tau$ for the relative sample.

**Table IV. Estimation of tortuosity through analytical formulations on the set of subvolumes for each CL. The average and standard deviation for each properties is reported, together with the corresponding value for the selected RVE.**

| | UBern-Ag | | TUDelft-Cu | | DTU-Cu | |
|---|---|---|---|---|---|---|
| | Ensemble | RVE | Ensemble | RVE | Ensemble | RVE |
| $\tau_B$ | 1.005 ± 0.002 | 1.005 | 1.025 ± 0.002 | 1.023 | 1.021 ± 0.003 | 1.025 |
| $\tau_M$ | 1.584 ± 0.001 | 1.584 | 1.596 ± 0.001 | 1.595 | 1.593 ± 0.002 | 1.596 |

**Table V. Tortuosity tensors components $\tau_i$ and the associated statistical analysis according to the data obtained from direct simulations.**

| | Mean | Standard deviation | Skewness | Minimum | Median | Maximum |
|---|---|---|---|---|---|---|
| UBern-Ag. $\tau_x$ | 1.021 | 0.007 | 2.217 | 1.010 | 1.020 | 1.084 |
| UBern-Ag. $\tau_y$ | 1.060 | 0.014 | 3.062 | 1.043 | 1.06 | 1.243 |
| UBern-Ag. $\tau_z$ | 1.019 | 0.007 | 1.747 | 1.009 | 1.017 | 1.058 |
| TUDelft-Cu. $\tau_x$ | 1.058 | 0.030 | 2.149 | 1.019 | 1.050 | 1.230 |
| TUDelft-Cu. $\tau_y$ | 1.151 | 0.052 | 0.502 | 1.046 | 1.141 | 1.324 |
| TUDelft-Cu. $\tau_z$ | 1.051 | 0.027 | 2.011 | 1.016 | 1.045 | 1.226 |
| DTU-Cu. $\tau_x$ | 1.133 | 0.091 | 0.656 | 1.023 | 1.108 | 1.374 |
| DTU-Cu. $\tau_y$ | 1.153 | 0.074 | 0.823 | 1.032 | 1.133 | 1.394 |
| DTU-Cu. $\tau_z$ | 1.108 | 0.071 | 0.757 | 1.022 | 1.089 | 1.325 |

CL. The Bruggeman formulation predicts much lower values for $\tau_B$ of the CLs, over 50% lower in all cases, while the difference between largest and smallest $\tau$ considering the same formulation is only few percentage points, and the difference between the distribution mean and the RVE is less than 1% in all cases.

The results obtained via pore-level simulations show that an analytically calculated $\tau_B$ tends to underestimate and $\tau_M$ tends to overestimate the tortuosity: direction-averaged $\tau$ in UBern-Ag is $\tau = 1.033$, for TUDelft-Cu is $\tau = 1.087$ and for DTU-Cu is $\tau = 1.131$. DTU-Cu exhibits the largest $\tau$, 9% larger than UBern-Ag. The differences among the CLs are more significant than implied by Bruggemann and Maxwell formulations, and the results clearly show that DTU-Cu is the sample with larger $\tau$ (as opposed to the analytical formulations showing similar behavior for TUDelft-Cu and DTU-Cu), highlighting the importance of morphological factors other than porosity on tortuosity. All the directly calculated average $\tau$ values tend to be closer to the Bruggeman estimations.

The directly calculated tortuosity distributions obtained from extracting streamlines' length from fluid flow calculations and plotted in Fig. 5 show non-normal distributions in every direction: the distributions are all positively skewed, and the KS test rejects the normal and the lognormal hypothesis (Table V). Skewness $s$ is calculated as in Eq. 8, where $sd$ is the standard deviation and $n = 60$ the number of sample points.

$$s = \frac{n}{(n-1)\cdot(n-2)} \sum_{i=1}^{n} \left( \frac{x_i - \bar{x}}{sd} \right)^3. \quad [8]$$

The directly calculated tortuosity clearly shows anisotropic behavior, which cannot be predicted with the analytical formulations. The mean tortuosity for the three CLs is always higher when considering a fluid flow along the $y$ direction: the highest anisotropic character is observed in the TUDelft-Cu sample, where $\tau_y$ is 9% higher than the average of $\tau_x$ and $\tau_z$. UBern-Ag $\tau_y$ is 4% higher than

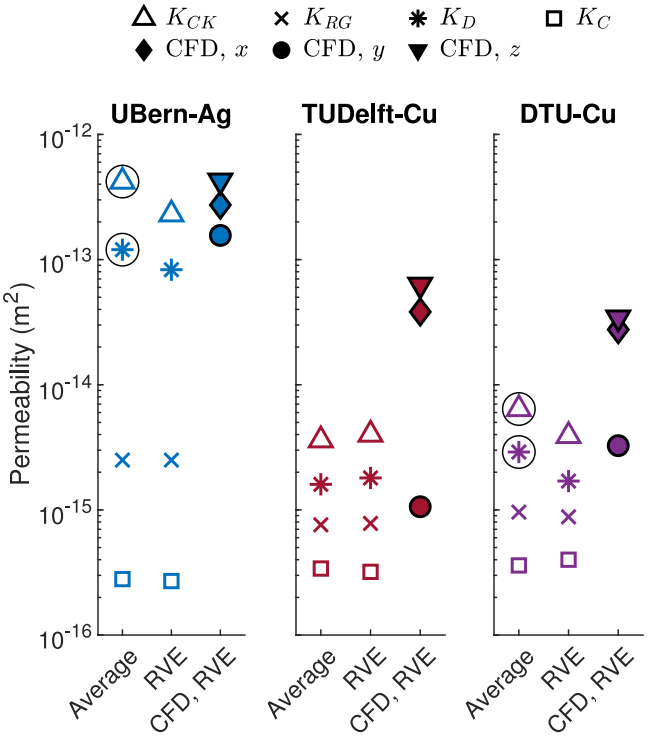


**Figure 6.** Comparison of average set permeability values obtained via a series of analytical formulation, values for permeability obtained applying the same formulations to the RVE and from direct pore-level simulations on the RVE for UBern-Ag, TUDelft-Cu and DTU-Cu. Data points highlighted by a gray circle correspond to distributions for which the normal hypothesis is rejected.

the average of $\tau_x$ and $\tau_z$, and the lowest anisotropy is exhibited by DTU-Cu, where $\tau_y$ is 3% higher than the average of $\tau_x$ and $\tau_z$. The directly calculated $\tau$ values follow the same trend in anisotropy as observed for the chord length distribution.

The CL with larger direction-averaged, simulations based $K = 2.85 \cdot 10^{-13}$ m$^2$ is UBern-Ag, due to its high $\varepsilon$ and low roughness factor. TUDelft-Cu and DTU-Cu direction-averaged $K$ are both one order of magnitude lower, respectively $3.41 \cdot 10^{-14}$ m$^2$ and $2.15 \cdot 10^{-14}$ m$^2$. $K$ is also estimated for all samples with the analytical formulations (Eq. 3—see Fig. 6). Note that not all the resulting distributions for the sets permeability estimation are normal (the KS test rejected in some cases the normal hypothesis). The estimations for which this is true were highlighted by a gray circle in Fig. 6, and a simple average of the set values, rather than the mean of the normal distribution with the corresponding $\sigma$, was reported. For each sample, a variation on a range of at least one order of magnitude can be observed for the analytical estimations of $K$. This variation does not correlate to the physical assumptions adopted in the models: in all cases, the largest $K$ is $K_{\mathrm{CK}}$, which is a formulation derived for packed spheres, followed by $K_{\mathrm{Davies}}$, which was derived for fibrous beds, $K_{\mathrm{RG}}$ (packed spheres), and finally by $K_{\mathrm{Chen}}$ (fibrous beds). In the case of TUDelft-Cu ($K_{\mathrm{CK}} = (3.6 \pm 0.7) \cdot 10^{-15}$ m$^2$, $K_{\mathrm{Davies}} = (1.6 \pm 0.3) \cdot 10^{-15}$ m$^2$, $K_{\mathrm{RG}} = (7.6 \pm 0.4) \cdot 10^{-16}$ m$^2$, $K_{\mathrm{Chen}} = (3.4 \pm 0.2) \cdot 10^{-16}$ m$^2$) and DTU-Cu ($K_{\mathrm{CK}} = 6.4 \cdot 10^{-15}$ m$^2$, $K_{\mathrm{Davies}} = 2.9 \cdot 10^{-15}$ m$^2$, $K_{\mathrm{RG}} = (9.6 \pm 0.6) \cdot 10^{-16}$ m$^2$, $K_{\mathrm{Chen}} = (3.6 \pm 0.4) \cdot 10^{-16}$ m$^2$), the average directly calculated $K$ is higher than $K_{\mathrm{CK}}$ by one order of magnitude, and higher than $K_{\mathrm{Chen}}$ by two orders of magnitude. Concerning UBern-Ag ($K_{\mathrm{CK}} = 4.2 \cdot 10^{-13}$ m$^2$, $K_{\mathrm{Davies}} = 1.2 \cdot 10^{-13}$ m$^2$, $K_{\mathrm{RG}} = (2.5 \pm 0.1) \cdot 10^{-15}$ m$^2$, $K_{\mathrm{Chen}} = (2.8 \pm 0.8) \cdot 10^{-16}$ m$^2$), the average directly calculated $K$ falls between $K_{\mathrm{CK}}$ and $K_{\mathrm{Davies}}$, and is three orders of magnitude higher than $K_{\mathrm{Chen}}$.

The directly calculated permeability tensors are given in Eq. 9.

$$\mathbf{K}_{\mathrm{UBern-Ag}} = \begin{pmatrix} 2.725 & 0 & 0 \\ 0 & 1.555 & 0 \\ 0 & 0 & 4.274 \end{pmatrix} \cdot 10^{-13}\ \mathrm{m}^2; \quad [9a]$$

$$\mathbf{K}_{\mathrm{TUDelft-Cu}} = \begin{pmatrix} 3.825 & 0 & 0 \\ 0 & 0.106 & 0 \\ 0 & 0 & 6.287 \end{pmatrix} \cdot 10^{-14}\ \mathrm{m}^2; \quad [9b]$$

$$\mathbf{K}_{\mathrm{DTU-Cu}} = \begin{pmatrix} 2.76 \pm 0.08 & 0 & 0 \\ 0 & 0.3 \pm 0.3 & 0 \\ 0 & 0 & 3.4 \pm 0.1 \end{pmatrix} \cdot 10^{-14}\ \mathrm{m}^2. \quad [9c]$$

All samples exhibit anisotropy in the permeability: the $K_y$ component is always lower than the $K_x$ and $K_z$ components. The sample with the highest degree of anisotropy is again TUDelft-Cu, with the average of the $x$ and $z$ components, $K_{xz}$, being 48 times $K_y$. In DTU-Cu, $K_{xz}$ is 10 times $K_y$. In UBern-Ag the anisotropy is less pronounced, with $K_{xz}$ being about twice $K_y$. Furthermore, although $K_y$ is the lowest-value component, the difference between $K_y$ and $K_x$ is smaller than between $K_z$ and $K_x$. The anisotropy trend is different than the one observed in the chord length distribution and $\boldsymbol{\tau}$, where DTU-Cu was the sample exhibiting a less anisotropic character. We explain this by noting that $\mathbf{K}$ depends not only on $\varepsilon$ but also on the material roughness factor and on the shape of the fluid path. The $K_y$ tensors component of TUDelft-Cu and DTU-Cu are better estimated by the analytical formulations: $K_y$ in TUDelft falls between the set mean $K_{\mathrm{Davies}}$ and $K_{\mathrm{RG}}$, while in DTU-Cu it falls between $K_{\mathrm{CK}}$ and $K_{\mathrm{Davies}}$. $K_{\mathrm{RG}}$ and $K_{\mathrm{C}}$ underestimate all $\mathbf{K}$ components in all cases. In the case of UBern-Ag, the high $\varepsilon$ and the low roughness factor may overpower the anisotropy of the solid domain and, at the same time, lead to higher $K$. The three components are well estimated by $K_{\mathrm{CK}}$ and $K_{\mathrm{Davies}}$, while $K_{\mathrm{RG}}$ and $K_{\mathrm{C}}$ underestimate all $\mathbf{K}$ components by different orders of magnitude.

The directly calculated normalized effective diffusion coefficient tensors are given in Eq. 10.

$$\left(\frac{\mathbf{D}_{\mathrm{eff}}}{D}\right)_{\mathrm{UBern-Ag}} = \begin{pmatrix} 0.970 & 0 & 0 \\ 0 & 0.960 & 0 \\ 0 & 0 & 0.987 \end{pmatrix}; \quad [10a]$$

$$\left(\frac{\mathbf{D}_{\mathrm{eff}}}{D}\right)_{\mathrm{TUDelft-Cu}} = \begin{pmatrix} 0.853 & 0 & 0 \\ 0 & 0.698 & 0 \\ 0 & 0 & 0.864 \end{pmatrix}; \quad [10b]$$

$$\left(\frac{\mathbf{D}_{\mathrm{eff}}}{D}\right)_{\mathrm{DTU-Cu}} = \begin{pmatrix} 0.89 \pm 0.03 & 0 & 0 \\ 0 & 0.77 \pm 0.02 & 0 \\ 0 & 0 & 0.90 \pm 0.03 \end{pmatrix}. \quad [10c]$$

The $y$ component of $\mathbf{D}_{\mathrm{eff}}/D$ is the lowest for all the CLs. TUDelft-Cu again shows the highest anisotropic behavior, with the $y$ component being 19% lower than the average of the $x$ and the $z$ components. DTU-Cu also shows an important degree of anisotropy, with its $y$ tensor component being 14% lower than the average of $x$ and $z$; while UBern-Ag $y$ component is only 2% lower than the average of $x$ and $z$, with the $x$ component being closer in value to the $y$ component than to the $z$ one. The trend is different than the one observed in the chord length distribution and $\boldsymbol{\tau}$, and it is the same observed as with $\mathbf{K}$. We explain it similarly by the fact that $D_{\mathrm{eff}}$ depends on both $\varepsilon$ and $\tau$, and again, the very high $\varepsilon$ of the sample seems to be dominating in this case.

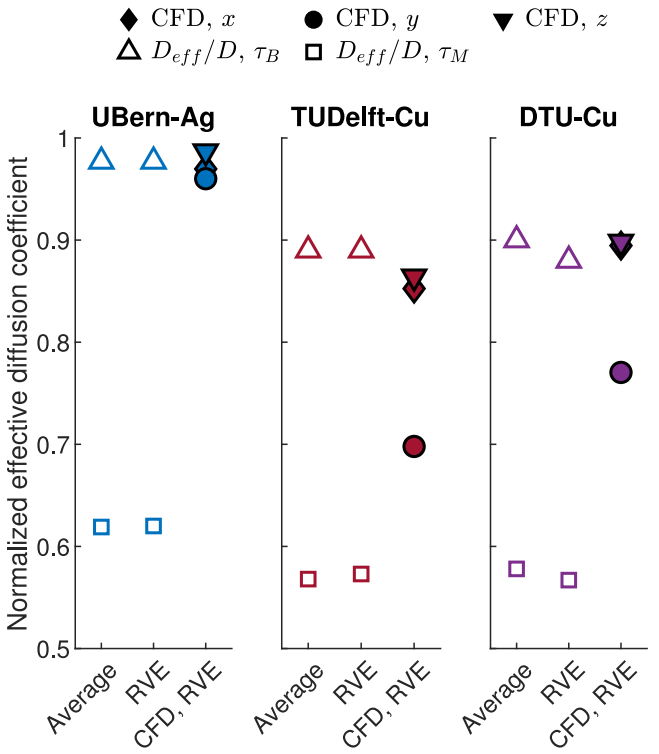


**Figure 7.** Comparison of average set normalized effective diffusion coefficient values obtained considering Maxwell and Bruggeman tortuosities, RVE analitical tortuosity results, and from direct pore-level simulations on the RVE for UBern-Ag, TUDelft-Cu and DTU-Cu samples.

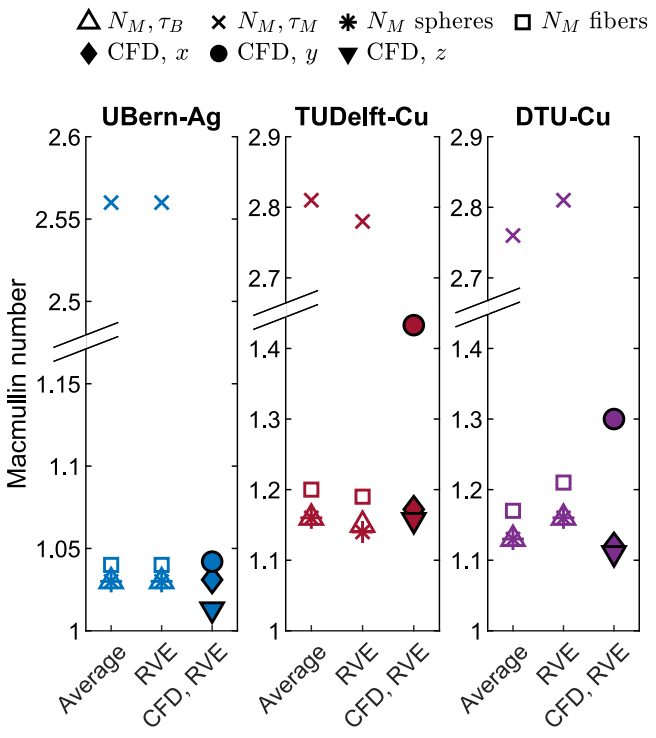


**Figure 8.** Comparison of the set average Macmullin number obtained considering different formulations, the RVE values calculated using the same formulations and the results obtained from direct pore-level simulations on the RVE for UBern-Ag, TUDelft-Cu and DTU-Cu samples.

$D_{\text{eff}}/D$ was also estimated by Eq. 4, considering both the Bruggeman and the Maxwell formulations. The average directly calculated $D_{\text{eff}}/D$ (0.972 for UBern-Ag, 0.805 for TUDelft-Cu and 0.85 for DTU-Cu) falls in between the two estimates for all CLs, as was the case for $\tau$: since $\tau_M$ overestimates the CLs tortuosities, the correspondent normalized diffusion coefficient is underestimated in all cases (mean $D_{\text{eff}}/D$ considering $\tau_M$ for the subvolumes set is $0.619 \pm 0.005$ for UBern-Ag, $0.568 \pm 0.005$ for TUDelft-Cu and $0.578 \pm 0.008$ for DTU-Cu), as can be seen in Fig. 7. The average directly calculated values are over 55% higher than the estimation considering $\tau_M$ in all cases. Conversely, since $\tau_B$ tends to underestimate the directly calculated $\tau$, $D_{\text{eff}}/D$ is on average underestimated, although the difference is very small for UBern-Ag, where the average directly calculated value is only 0.5% lower than the estimate considering $\tau_B$ ($D_{\text{eff}}/D = 0.977 \pm 0.009$). In the case of TUDelft-Cu and DTU-Cu, the average directly calculated $D_{\text{eff}}/D$ is, respectively, 10% and 5% lower than the estimate considering $\tau_B$ ($D_{\text{eff}}/D = 0.89 \pm 0.01$ and $0.90 \pm 0.01$, respectively). Nevertheless, the $D_{\text{eff}}/D$ estimates calculated from $\tau_B$ are in good agreement with the directly calculated $x$ and $z$ components of the TUDelft-Cu and DTU-Cu CLs: the average value for $D_{\text{eff},xz}/D$ is respectively 0.859 and 0.895, only 3.5% and 0.6% lower than the Bruggeman estimate. In turn, $D_{\text{eff},y}/D$ for the two CLs are 22% and 14% lower than the Bruggeman estimate –23% and 33% higher than the Maxwell estimate.

We note that the effect of the porous structure would be the same when considering Stefan-Maxwell diffusivity: $D$ in Eq. 10 would represent the Stefan-Maxwell diffusion coefficients. Furthermore, one could consider an ionomer filling the pores: in this case, $D$ in Eq. 10 would represent the diffusion coefficient of the species in the ionomer.

The normalized effective ionic conductivity $\boldsymbol{\sigma}_{\text{eff}}/\sigma$ is the same as $\mathbf{D}_{\text{eff}}/D$ (see Eq. 7). The reciprocal of the quantity is given for all CLs in Eq. 11 to allow for direct comparison with $N_M$ obtained from different formulations (Eq. 5—see Fig. 8).

$$\left(\frac{\sigma}{\boldsymbol{\sigma}_{\text{eff}}}\right)_{\text{UBern-Ag}} = \begin{pmatrix} 1.031 & 0 & 0 \\ 0 & 1.042 & 0 \\ 0 & 0 & 1.013 \end{pmatrix}; \quad [11a]$$

$$\left(\frac{\sigma}{\boldsymbol{\sigma}_{\text{eff}}}\right)_{\text{TUDelft-Cu}} = \begin{pmatrix} 1.172 & 0 & 0 \\ 0 & 1.433 & 0 \\ 0 & 0 & 1.157 \end{pmatrix}; \quad [11b]$$

$$\left(\frac{\sigma}{\boldsymbol{\sigma}_{\text{eff}}}\right)_{\text{DTU-Cu}} = \begin{pmatrix} 1.12 \pm 0.03 & 0 & 0 \\ 0 & 1.30 \pm 0.03 & 0 \\ 0 & 0 & 1.11 \pm 0.03 \end{pmatrix}. \quad [11c]$$

As in the case of $\mathbf{D}_{\text{eff}}/D$, the sample showing the higher anisotropy is TUDelft-Cu, with the $y$ tensor component being 23% higher than $xz$ (the average of $x$ and $z$ components), followed by DTU-Cu, with a $y$ component 16% higher than $xz$, and finally UBern-Ag, where the $y$ component is the highest one, but it is only 2% higher than $xz$, and with the $x$ component being closer to $y$ than to $z$. $N_M$ estimations considering $\tau_M$ widely overestimate the directly calculated values (Fig. 8): $N_M$ mean for the sets is estimated as $2.56 \pm 0.02$ for UBern-Ag, $2.81 \pm 0.03$ for TUDelft-Cu and $2.76 \pm 0.04$ for DTU-Cu, respectively 2.5, 2.2 and 2.3 times more than the average directly calculated values ($N_M = 1.029$ for UBern-Ag, 1.254 for TUDelft-Cu and 1.177 for DTU-Cu). The other $N_M$ estimations are in better agreement with the directly calculated values: in the case of UBern-Ag the difference is below 1% in all cases ($N_{M,\tau B} = 1.03 \pm 0.01$, $N_{M,\text{spheres}} = 1.03 \pm 0.01$ and $N_{M,\text{fibers}} = 1.04 \pm 0.01$). Also in the case of TUDelft-Cu ($N_{M,\tau B} = 1.16 \pm 0.02$, $N_{M,\text{spheres}} = 1.16 \pm 0.01$ and $N_{M,\text{fibers}} = 1.20 \pm 0.02$) and DTU-Cu ($N_{M,\tau B} = 1.13 \pm 0.02$, $N_{M,\text{spheres}} = 1.13 \pm 0.02$ and $N_{M,\text{fibers}} = 1.17 \pm 0.03$) the estimations are in good agreement, with $N_{M,\tau B}$ and $N_{M,\text{spheres}}$ being 7% lower

**Table VI. Estimation of solid tortuosity through analytical formulations and the corresponding normalized effective electronic conductivity on the set of subvolumes for each CL. The average and standard deviation for each properties is reported, together with the corresponding value for the selected RVE.**

| | UBern-Ag | | TUDelft-Cu | | DTU-Cu | |
|---|---|---|---|---|---|---|
| | Ensemble | RVE | Ensemble | RVE | Ensemble | RVE |
| $\tau_{s,B}$ | 2.7 ± 0.3 | 2.711 | 1.81 ± 0.04 | 1.844 | 1.90 ± 0.07 | 1.803 |
| $\sigma^e_{\text{eff}}/\sigma^e$, $\tau_{s,B}$ | 0.007 ± 0.003 | 0.007 | 0.051 ± 0.005 | 0.047 | 0.042 ± 0.007 | 0.052 |
| $\tau_{s,M}$ | 1.729 ± 0.008 | 1.729 | 1.719 ± 0.001 | 1.720 | 1.721 ± 0.002 | 1.718 |
| $\sigma^e_{\text{eff}}/\sigma^e$, $\tau_{s,M}$ | 0.011 ± 0.004 | 0.011 | 0.054 ± 0.005 | 0.050 | 0.046 ± 0.006 | 0.055 |

than the directly calculated $N_M$ for TUDelft-Cu and 4% lower for DTU-Cu, and $N_{M,\text{fibers}}$ being 4% and 0.6% lower than the average directly calculated value for TUDelft-Cu and DTU-Cu, respectively. The $y$ tensor component of TUDelft-Cu is 24% higher than $N_{M,\tau B}$ and $N_{M,\text{spheres}}$, while the difference with respect to the $x$ and $z$ components is less than 1%. $xz$ difference with respect to $N_{M,\text{fibers}}$ is 3%, while the $y$ component is 19% higher. In the case of DTU-Cu the $y$ component is 15% higher than $N_{M,\tau B}$ and $N_{M,\text{spheres}}$ and 11% higher than $N_{M,\text{fibers}}$, while the $x$ and $z$ component are again in better agreement with the estimations, with their average being 1% lower than $N_{M,\tau B}$ and $N_{M,\text{spheres}}$ and 5% lower than $N_{M,\text{fibers}}$.

The solid tortuosity $\tau_s$ and the normalized effective electronic conductivity $\sigma^e_{\text{eff}}/\sigma^e$ were estimated considering Maxwell and Bruggeman formulations, see Table VI. Unlike in the case of $\tau$, the values estimated by the Maxwell formulation for $\tau_s$ are lower than the predictions from Bruggeman formulation. UBern-Ag is the sample with higher $\tau_s$: $\tau_{s,B} = 2.7 \pm 0.3$, a value 56% larger than $\tau_{s,M} = 1.729 \pm 0.008$. The $\tau_{s,M}$ values calculated for DTU-Cu and TUDelft-Cu ($1.721 \pm 0.002$ and $1.719 \pm 0.001$) are only less than 1% lower, which seems unreasonable given the extremely low $\phi$ of UBern-Ag. The Bruggeman formulation predicts $\tau_{s,B} = 1.90 \pm 0.07$ and $1.81 \pm 0.04$ for respectively DTU-Cu and TUDelft-Cu, 10% and 5% more than the corresponding $\tau_{s,M}$ values and, more importantly, 30% and 33% less than UBern-Ag $\tau_{s,B}$. Consequently, the $\sigma^e_{\text{eff}}/\sigma^e$ values estimated starting from $\tau_{s,B}$ are lower than the ones considering $\tau_{s,M}$. The sample with lower estimated $\sigma^e_{\text{eff}}/\sigma^e$ is UBern-Ag ($0.007 \pm 0.003$ considering $\tau_{s,B}$ and $0.011 \pm 0.004$ considering $\tau_{s,M}$), which is one order of magnitude lower than DTU-Cu ($0.051 \pm 0.005$ considering $\tau_{s,B}$; $0.054 \pm 0.005$ considering $\tau_{s,M}$) and TUDelft-Cu ($0.042 \pm 0.007$ considering $\tau_{s,B}$; $0.046 \pm 0.006$ considering $\tau_{s,M}$). UBern-Ag is also the sample for which the two estimates are more distant: $\sigma^e_{\text{eff}}/\sigma^e$ considering $\tau_{s,B}$ is 57% lower than the $\tau_{s,M}$ estimation. This difference is only 10 and 6% for TUDelft-Cu and DTU-Cu, respectively.

$\boldsymbol{\sigma}^e_{\text{eff}}/\sigma^e$ was directly calculated for the TUDelft-Cu sample. Numerical difficulties were encountered when simulating electrons diffusion in the UBern-Ag and DTU-Cu CLs. The solutions did not satisfy convergence criteria and were deemed unphysical. Results for TUDelft-Cu are given in Eq. 12.

$$\left(\frac{\boldsymbol{\sigma}^e_{\text{eff}}}{\sigma^e}\right)_{\text{TUDelft-Cu}} = \begin{pmatrix} 2.35 & 0 & 0 \\ 0 & 0.62 & 0 \\ 0 & 0 & 3.69 \end{pmatrix} \cdot 10^{-2}. \quad [12]$$

The average directly calculated $\sigma^e_{\text{eff}}/\sigma^e$ corresponds to $2.22 \cdot 10^{-2}$, respectively 48% and 52% less than the estimation considering $\tau_{s,B}$ and $\tau_{s,M}$. The $y$ tensor component is 79% lower than the average of $x$ and $z$ components, and it is 85% and 87% lower than the $\tau_{s,B}$ and $\tau_{s,M}$-based estimations. The average $xz$ component is closer to the estimates, but still 28% and 34% lower, respectively.

## Conclusions

Homogenized modeling of GDE-based devices for electrochemical $CO_2$ reduction offers a computationally efficient approach to describe the physical processes occurring in complex devices without the complexity of pore-scale modeling. However, the accuracy of such models relies heavily on a set of descriptors of the morphological and effective transport properties of the materials composing the GDE. Typically, these descriptors are estimated using analytical formulations based on simple properties such as porosity, and rely heavily on assumptions about pore-scale morphology. In particular, isotropy is always assumed. We obtained a set of descriptors derived from direct (pore-level) numerical simulations of three different CLs for $CO_2$RR. These CLs were digitized by FIB-SEM nano-tomography and subsequent segmentation.

This work allowed to obtain quantitative information on the CL of two sputtered Cu-based GDEs and one Ag particle deposition-based GDE, providing a reliable dataset of mesoscale properties that can be used to accurately model GDE-based devices. In-depth quantitative morphological characterization allowed to obtain a comprehensive set of morphological descriptors ($\varepsilon$, $\phi$, volume fraction profile, average particle diameter, roughness factor, connected volume, chord length distribution). The RVEs were then meshed with inlet and outlet along the three Cartesian principal axes and the relevant governing Eqs. were solved at the pore scale to obtain $\boldsymbol{\tau}$, $\mathbf{K}$, $\mathbf{D}_{\text{eff}}/D$, $\boldsymbol{\sigma}_{\text{eff}}/\sigma$ and $\boldsymbol{\sigma}^e_{\text{eff}}/\sigma^e$. Obtaining effective properties in the form of tensors allowed to directly account for anisotropy.

Our results show that analytically derived formulations often fail to accurately predict the morphological and effective transport properties, in some cases by orders of magnitude. Furthermore, the effective properties of CLs vary significantly depending on the transport direction considered: the integration of anisotropy in the homogenized modeling of GDE-based devices is crucial for a more realistic representation of their behavior. We believe that most of the experimentally produced CL are implicitly anisotropic, and this characteristic was not consistently included in homogenized modelling of GDE-based devices up to now. Considering our results, we emphasize the need to be cautious when assuming pore-scale geometry and relying solely on analytical formulations to estimate effective transport properties. Instead, we recommend the use of mesoscale-derived data whenever possible. If this is not feasible, we recommend testing the effect of anisotropy in finalized models, conducting sensitivity studies and considering a range of possible values for the transport properties.

## Acknowledgments

This project has received funding from the European Union's Horizon 2020 research and innovation programme under the Marie-Skłodowska-Curie grant agreement No. 861151 and under grant agreement SELECTCO2 No. 851441. This publication was created as part of NCCR Catalysis (grant number 180544), a National Centre of Competence in Research funded by the Swiss National Science Foundation. We thank Tom Burdyny at TU Delft, Brian Seger at DTU and Peter Broekmann at University of Bern for sharing catalyst layers. We thank Silvan Suter (former EPFL) and Lucie Navratilova for support in imaging with FIB-SEM nanotomography.

## ORCID

Francesca Lorenzutti https://orcid.org/0000-0002-3459-2425
Sophia Haussener https://orcid.org/0000-0002-3044-1662

## References

1. W. Tang, A. A. Peterson, A. S. Varela, Z. P. Jovanov, L. Bech, W. J. Durand, S. Dahl, J. K. Nørskov, and I. B. Chorkendorff, "The importance of surface morphology in controlling the selectivity of polycrystalline copper for $CO_2$ electroreduction." *Phys. Chem. Chem. Phys.*, **14**, 76 (2012).
2. A. S. Hall, Y. Yoon, A. Wuttig, and Y. Surendranath, "Mesostructure-induced selectivity in $CO_2$ reduction catalysis." *J. Am. Chem. Soc.*, **137**, 14834 (2015).
3. A. Dutta, M. Rahaman, N. C. Luedi, M. Mohos, and P. Broekmann, "Morphology matters: tuning the product distribution of $CO_2$ electroreduction on oxide-derived Cu foam catalysts." *ACS Catal.*, **6**, 3804 (2016).
4. J. Qi, W. Zhang, and R. Cao, "Porous materials as highly efficient electrocatalysts for the oxygen evolution reaction." *ChemCatChem*, **10**, 1206 (2018).
5. D. Higgins, C. Hahn, C. Xiang, T. F. Jaramillo, and A. Z. Weber, "Gas-diffusion electrodes for carbon dioxide reduction: a new paradigm." *ACS Energy Lett.*, **4**, 317 (2019).
6. W. A. Smith, T. Burdyny, D. A. Vermaas, and H. Geerlings, "Pathways to industrial-scale fuel out of thin air from $CO_2$ electrolysis." *Joule*, **3**, 1822 (2019).
7. J. C. Bui, E. W. Lees, L. M. Pant, I. V. Zenyuk, A. T. Bell, and A. Z. Weber, "Continuum modeling of porous electrodes for electrochemical synthesis." *Chem. Rev.*, **122**, 11022 (2022).
8. L.-C. Weng, A. T. Bell, and A. Z. Weber, "Modeling gas-diffusion electrodes for $CO_2$ reduction." *Phys. Chem. Chem. Phys.*, **20**, 16973 (2018).
9. L.-C. Weng, A. T. Bell, and A. Z. Weber, "Towards membrane-electrode assembly systems for $CO_2$ reduction: a modeling study." *Energy & Environmental Science*, **12**, 1950 (2019).
10. M. R. Singh, E. L. Clark, and A. T. Bell, "Effects of electrolyte, catalyst, and membrane composition and operating conditions on the performance of solar-driven electrochemical reduction of carbon dioxide." *Phys. Chem. Chem. Phys.*, **17**, 18924 (2015).
11. S. Suter and S. Haussener, "Optimizing mesostructured silver catalysts for selective carbon dioxide conversion into fuels." *Energy Environ. Sci.*, **12**, 1668 (2019).
12. E. M. Ryan and P. P. Mukherjee, "Mesoscale modeling in electrochemical devices–a critical perspective." *Progress in Energy and Combustion Science*, **71**, 118 (2019).
13. S. Suter, M. Cantoni, Y. K. Gaudy, S. Pokrant, and S. Haussener, "Linking morphology and multi-physical transport in structured photoelectrodes." *Sustainable Energy & Fuels*, **2**, 2661 (2018).
14. F. Cadiou, T. Douillard, F. Willot, J. C. Badot, B. Lestriez, and E. Maire, "Effective electronic and ionic conductivities of dense EV-designed NMC-based positive electrodes using fourier based numerical simulations on FIB/SEM volumes." *J. Electrochem. Soc.*, **167**, 140504 (2020).
15. M. Ma, E. L. Clark, K. T. Therkildsen, S. Dalsgaard, I. B. Chorkendorff, and B. Seger, "Insights into the carbon balance for $CO_2$ electroreduction on Cu using gas diffusion electrode reactor designs." *Energy & Environmental Science*, **13**, 977 (2020), Publisher: Royal Society of Chemistry.
16. M. Ma, S. Kim, I. B. Chorkendorff, and B. Seger, "Role of ion-selective membranes in the carbon balance for $CO_2$ electroreduction via gas diffusion electrode reactor designs." *Chemical Science*, **11**, 8854 (2020), Publisher: Royal Society of Chemistry.
17. N. J. Firet, T. Burdyny, N. T. Nesbitt, S. Chandrashekar, A. Longo, and W. A. Smith, "Copper and silver gas diffusion electrodes performing $CO_2$ reduction studied through operando X-ray absorption spectroscopy." *Catalysis Science & Technology*, **10**, 5870 (2020), Publisher: Royal Society of Chemistry.
18. Y. Kong, M. Liu, H. Hu, Y. Hou, S. Vesztergom, M. de Jesus Gálvez-Vázquez, I. Zelocualtecatl Montiel, V. Kolivoška, and P. Broekmann, "Cracks as efficient tools to mitigate flooding in gas diffusion electrodes used for the electrochemical reduction of carbon dioxide." *Small Methods*, **6**, 2200369 (2022).
19. I. Utke, S. Moshkalev, and P. Russell, *Nanofabrication using Focused ion and Electron Beams : Principles and Applications* (Oxford University Press, New York) Nanomanufacturing series, Chap. 11 (2012).
20. J. C. Russ, *The Image Processing Handbook* (CRC Press) (2006).
21. E. A. Wargo, A. C. Hanna, A. Een, S. R. Kalidindi, and E. C. Kumbur, "Selection of representative volume elements for pore-scale analysis of transport in fuel cell materials." *Journal of Power Sources*, **197**, 168 (2012).
22. A. Çeçen, E. A. Wargo, A. C. Hanna, D. M. Turner, S. R. Kalidindi, and E. C. Kumbur, "3-D microstructure analysis of fuel cell materials: spatial distributions of tortuosity, void size and diffusivity." *J. Electrochem. Soc.*, **159**, B299 (2012).
23. S. Torquato, *Random Heterogeneous Materials: Microstructure and Macroscopic Properties* (Springer, New York, NY) vol. 16 (2002), Interdisciplinary Applied Mathematics, 2nd print 10.1007/978-1-4757-6355-3.
24. B. Tjaden, D. J. L. Brett, and P. R. Shearing, "Tortuosity in electrochemical devices: a review of calculation approaches." *International Materials Reviews*, **63**, 47 (2018).
25. D. A. G. Bruggeman, "Berechnung verschiedener physikalischer konstanten von heterogenen substanzen. I. dielektrizitätskonstanten und leitfähigkeiten der mischkörper aus isotropen substanzen." *Ann. Phys. (Berlin)*, **416**, 636 (1935).
26. B. Tjaden, S. J. Cooper, D. J. L. Brett, D. Kramer, and P. R. Shearing, "On the origin and application of the bruggeman correlation for analysing transport phenomena in electrochemical systems." *Current Opinion in Chemical Engineering*, **12**, 44 (2016).
27. M. Kaviany, *Principles of Heat Transfer in Porous Media* (Springer, New York) 2nd ed. (1995), Mechanical engineering series.
28. H. C. H. Rumpf and A. R. Gupte, "Einflüsse der porosität und korngrößenverteilung im widerstandsgesetz der porenströmung." *Chem. Ing. Tech.*, **43**, 367 (1971).
29. F. A. L. Dullien, *Porous Media, Fluid Transport and Pore Structure* (Academic Press, San Diego, CA) (1979).
30. C. Y. Chen, "Filtration of aerosols by fibrous media." *Chem. Rev.*, **55**, 595 (1955).
31. N. Epstein, "On tortuosity and the tortuosity factor in flow and diffusion through porous media." *Chemical Engineering Science*, **44**, 777 (1989).
32. M. J. Martínez, S. Shimpalee, and J. W. Van Zee, "Measurement of MacMullin numbers for PEMFC gas-diffusion media." *J. Electrochem. Soc.*, **156**, B80 (2009).
33. R. B. MacMullin and G. A. Muccini, "Characteristics of porous beds and structures." *AIChE Journal an Official Publication of the American Institute of Chemical Engineers*, **2**, 393 (1956).
34. M. M. Tomadakis and S. V. Sotirchos, "Ordinary and transition regime diffusion in random fiber structures." *AIChE J.*, **39**, 397 (1993).
35. K. Zheng, Y. Zhang, L. Li, and M. Ni, "On the tortuosity factor of solid phase in solid oxide fuel cell electrodes." *International Journal of Hydrogen Energy*, **40**, 665 (2015).
36. H. G. Weller, G. Tabor, H. Jasak, and C. Fureby, "A tensorial approach to computational continuum mechanics using object-oriented techniques." *Comput. Phys.*, **12**, 620 (1998).
37. J. Schwartz et al., "Real-Time 3D Analysis during Electron Tomography Using Tomviz." *Nature Communications*, **13** (2022).